Designing Three-Dimensional Architectures for High-Performance Electron Accepting Pseudocapacitors

Samuel R. Peurifoy,[†,§] Jake C. Russell,[†,§] Thomas J. Sisto,[§] Yuan Yang,*[,‡] Xavier Roy,*[,§] and Colin Nuckolls*[,§]

[§]Department of Chemistry, Columbia University, New York, New York 10027, United States

[‡]Program of Materials Science and Engineering, Department of Applied Physics and Applied Mathematics, Columbia University, New York, New York 10027, United States

Ⓢ *Supporting Information*

ABSTRACT: By storing energy from electrochemical processes at the electrode surface, pseudocapacitors bridge the performance gap between electrostatic double-layer capacitors and batteries. In this context, molecular design offers the exciting possibility to create tunable and inexpensive organic electroactive materials. Here we describe a porous structure composed of perylene diimide and triptycene subunits and demonstrate its remarkable performance as a pseudocapacitor electrode material. The material exhibits capacitance values as high as 350 F/g at 0.2 A/g as well as excellent stability over 10 000 cycles. Moreover, we can alter the performance of the material, from battery-like (storing more charge at low rates) to capacitor-like (faster charge cycling), by modifying the structure of the pores via flow photocyclization. Organic materials capable of stable electron accepting pseudocapacitor behavior are rare and the capacitance values presented here are among the highest reported. More broadly, this work establishes molecular design and synthesis as a powerful approach for creating tunable energy storage materials.

The development of new materials capable of storing and rapidly distributing energy is essential for keeping pace with emerging renewable energy production technologies. Together, capacitor and battery devices underpin most electrical energy storage systems—the former for rapid charge/discharge cycling, and the latter for long-term energy storage. Pseudocapacitors incorporate elements of both batteries and capacitors, exhibiting a linear dependence of charge stored versus potential as a consequence of surface-level Faradaic electron-transfer processes.[1] These devices have gained popularity for applications requiring charge storage at intermediate time scales, such as regenerative braking in electric vehicles. High-performance pseudocapacitors are typically made from inorganic solid state compounds with limited synthetic tunability.[2,3] Organic materials are attractive because they offer a modular framework paired with mild processing conditions. Most organic pseudocapacitor materials, however, are electron donating (i.e., *p*-type),[4,5] meaning the charge storage process is oxidative; in general, electron accepting (i.e., *n*-type) materials exhibit low capacitance, poor electrochemical stability and high resistivity.[6−9] To achieve the widest potential range and highest practical capacitance, both electron accepting and electron donating materials are required to fabricate pseudocapacitor devices.[7]

In this work, we describe a new porous architecture constructed from perylene diimide (PDI) and triptycene subunits, and establish its outstanding performance as an *n*-type pseudocapacitor material.[10] A common dye and pigment, PDI has received widespread attention due to its attractive chemical and electrochemical properties for molecular electronics,[11] photovoltaics,[12] batteries[13] and photocatalytic applications.[14] By coupling PDI to a subunit possessing considerable internal free volume, we create a material with high internal surface area and thermal stability. These structural properties, combined with the robust redox behavior of the PDI subunit, produce *n*-type pseudocapacitance of 350 F/g, excellent performances at a current density as high as 10 A/g, and stability for >10 000 cycles alongside a Coulombic efficiency of >98%. These results are among the highest values reported to date for an organic *n*-type pseudocapacitor material.[15−17] Furthermore, our molecular design allows us to modify the structure of the scaffold by cyclizing the backbone via flow photocyclization. This modification produces significant changes in the pseudocapacitive performance of the material, converting it from a more battery-like behavior to a more capacitor-like behavior.

Figure 1 presents the two monomers used to create the porous scaffold through a Pd-catalyzed Suzuki polymerization. The triptycene unit is synthesized by using C−H activation chemistry to achieve a one-step borylation of triptycene.[12] The synthetic details for the synthesis of 1,7-dibromoPDI have been reported.[18] The Suzuki copolymerization of these monomers yields the insoluble polymeric material **1**. N₂ adsorption isotherms indicate that the material possesses a small internal surface area (15 m²/g) because the alkyl chains occupy the pores (Figure S1a).

These chains, however, can be removed from the pores by thermolysis. Thermogravimetric analysis (TGA) of **1** illustrates this process: ~40% of the sample mass, corresponding to the mass of the alkyl chains, is lost at ~400 °C (Figure 2a). To remove the chains, **1** is sealed under vacuum in a glass tube and heated to 400 °C in a tube furnace for 2 h, leaving one end
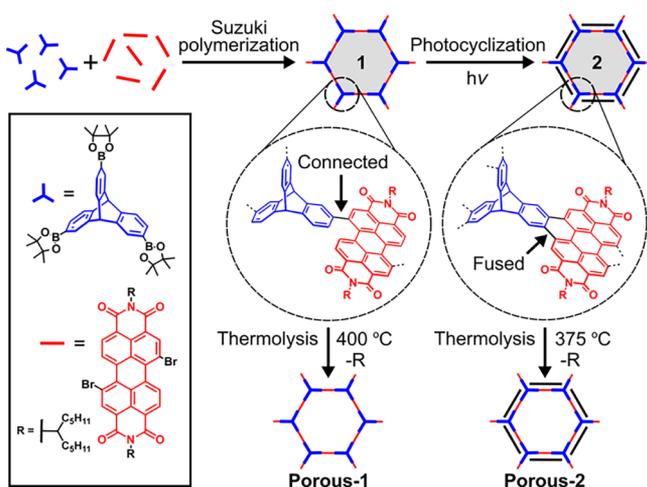
Figure 1. Schematic showing one idealized hexagonal macrocyclic pore subunit and the molecular structures of its building blocks. The PDI-triptycene linkages in **1** and **Porous-1** are a mixture of isomers. The single lines in the schematic indicate covalent connection and the double lines indicate fusion of the subunits.
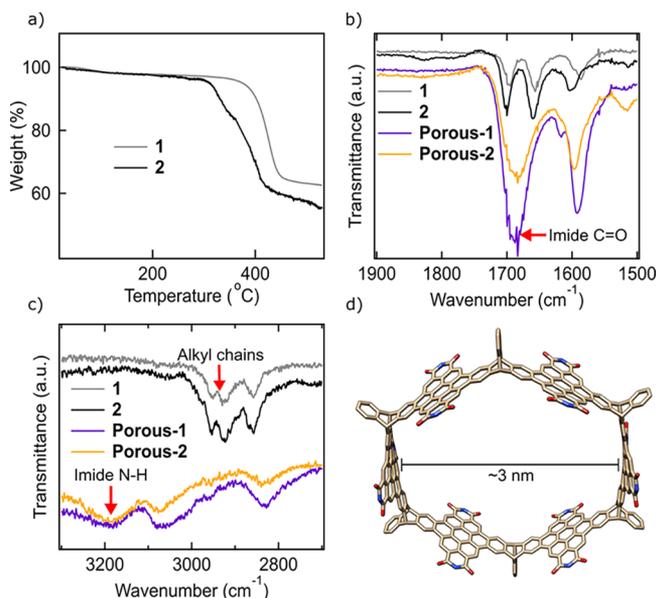

Figure 2. (a) TGA of **1** and **2**. (b) IR spectra of **1**, **2**, **Porous-1** and **Porous-2**, showing the carbonyl region. The imide C=O peaks (1690 cm^{-1}) are retained following thermolysis. (c) IR spectra of **1**, **2**, **Porous-1** and **Porous-2**, showing the alkyl spectral region. The alkyl peaks (3050–2800 cm^{-1}) are lost upon thermolysis, and an imide N—H peak (~3150 cm^{-1}) appears. (d) DFT-optimized energy minimum structure of a truncated fused macrocyclic subunit.

of the tube cold. The condensate at the cold end is primarily undecene (Figure S2). The thermolyzed solid, **Porous-1**, has a significantly larger surface area (71 m^2/g) than **1**. Infrared (IR) spectroscopy indicates the presence of primary imides in the thermolyzed solid and confirms the loss of vibrational modes from the alkyl groups (Figure 2b,c; Figure S3).[19]

A soluble low molecular weight material (**1′**) can be prepared by reducing the concentration of the reagents in the reaction to slow down the rate of polymerization. This soluble material is then photocyclized in solution using visible light to yield **2**.[20] NMR spectroscopy verifies the cyclization: resonances assigned to protons from uncyclized **1′** are absent

in the spectrum of **2** (Figures S4, S5),[12,21] and the optical absorption characteristics exhibit sharpened λ_{max} band edges (Figure S8). Similar to **1**, compound **2** can be heated to 375 °C to remove the alkyl chains from the pores, increasing the internal surface area of the material from 16 m^2/g for **2** to 185 m^2/g for **Porous-2**. Note that **Porous-2** has a larger surface area than **Porous-1** because the photocyclization stiffens the structure and increases the aromatic surface area.

The proposed structure of **Porous-2** can be visualized with density functional theory (DFT) calculations of a single truncated macrocycle,[22] which indicate that the pore diameter should be ~3 nm (Figure 2d). These calculations support the pore size distribution calculated from the N$_2$ adsorption isotherm data.[23] (Figure S1b). The powder X-ray diffraction patterns of all the materials are typical of disordered mesoporous materials: they feature a broad low-angle peak with *d*-spacings corresponding to the pore diameter (Figure S6).[24,25]

To investigate the electrochemical properties of the porous scaffold, we fabricate electrodes by depositing a slurry of **Porous-1** or **Porous-2**, carbon black (10 wt %), and polytetrafluoroethylene (10 wt %) onto Ni foam.[26] All electrochemical analyses are performed in 1 M Na$_2$SO$_4$ aqueous electrolyte solution with a Pt counter electrode and a Ag/AgCl reference electrode.

The electrochemical behavior of **Porous-1** and **Porous-2** combines electrostatic double-layer capacitance and Faradaic characteristics. This behavior, defined as pseudocapacitance,[1] arises from surface-level charge transfer to the PDI subunits that are accessible as a result of the porous scaffolding with triptycene. In general, **Porous-1** performs better at low charging rates and **Porous-2** performs better at higher rates; this change in behavior is a direct consequence of their structural differences. As expected, the materials before removal of the side chains (**1** and **2**) display poor electrochemical performance, with low capacitance and high resistance due to the insulating alkyl chains in the pores (Figure S10). After thermolysis, the performance of both materials greatly improves.

Figure 3a−d presents cyclic voltammograms (CVs) of **Porous-1** and **Porous-2** at various scan rates. Both materials display a broad reversible redox couple at negative potential, whose shape is typical of neither a purely Faradaic peak nor a supercapacitor rectangular response.[7,27] The negative bias and broadening of the couple results from surface-level reversible reduction processes.

At low scan rates, the broad peak resolves into two distinct events (Figure 3b,d), assigned to the sequential reduction of the two diimide moieties on the PDI subunit.[11,12,20] The potential of these two events agree with those of a control device fabricated with PDI only (Figure S10c), as well as with the behavior of a model compound made of three PDIs linked to a triptycene central unit.[12] These results indicate that the electrochemical behavior of **Porous-1** and **Porous-2** arises from reductive processes at the PDI units.

The specific capacitance (*C*) of **Porous-1** and **Porous-2** is calculated from the galvanostatic charge−discharge (GCD) curves at various current densities (Figure 3e−h) using eq 1:

$$C = \frac{i \cdot t}{m \cdot \Delta E}$$

(1)

where *i* is current, *t* is discharge cycle time, *m* is mass of active material, and ΔE is potential difference. These curves have the
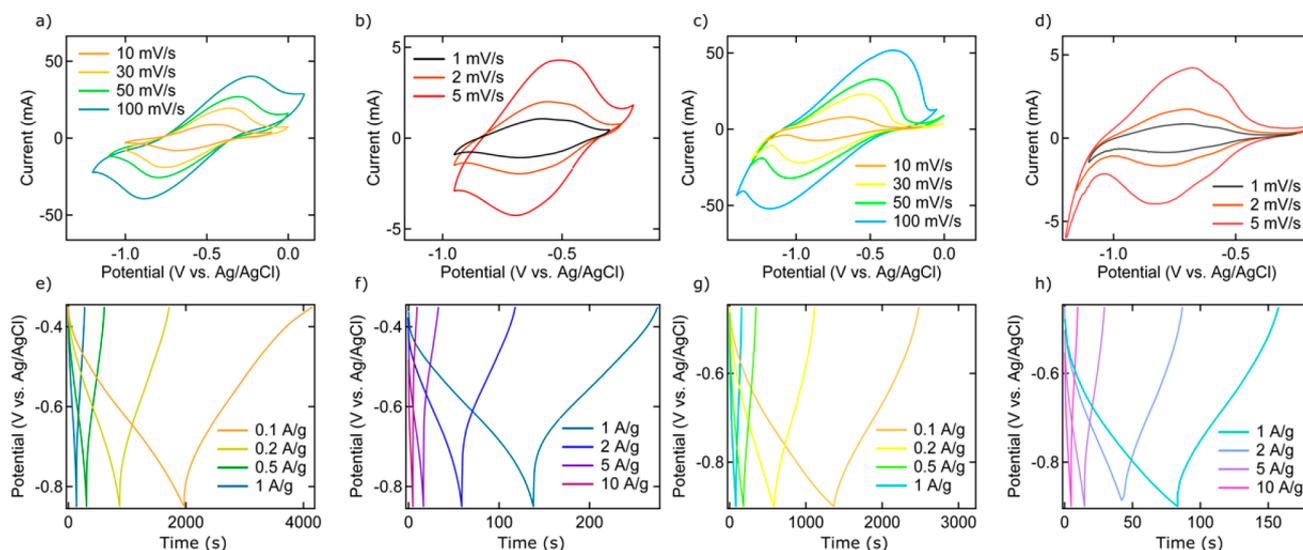
Figure 3. (a and b) CVs of **Porous-1** at (a) high and (b) low scan rates. (c and d) CVs of **Porous-2** at (c) high and (d) low scan rates. (e and f) GCD curves of **Porous-1** at (e) high and (f) low currents. (g and h) GCD curves of **Porous-2** at (g) high and (h) low currents.

symmetric triangular shape typical of capacitive behavior,[7] with a small nonlinear component due to pseudocapacitance.

Specific capacitance for a range of current densities is shown in Figure 4a. At the lowest current density (0.2 A/g), **Porous-1** has a capacitance of 352 F/g, one of the highest reported values for stable *n*-type organic materials.[15−17] The corre-

Figure 4. (a) Specific capacitance of **Porous-1** and **Porous-2** as a function of current density. (b) Cycling stability of **Porous-1** and **Porous-2** at a current density of 5 A/g. (c) Nyquist plot of **Porous-1** and **Porous-2**, from 10 kHz to 5 mHz. Inset shows the high-frequency region (10 kHz to 100 Hz). Arrows indicate frequencies for reference. (d) Specific capacitance as a function of frequency.

sponding specific capacity is 59 mAh/g. These values approach the theoretical specific capacitance[28] (548 F/g) and capacity (84 mAh/g) of the material, indicating that ∼70% of the redox sites are accessible. The capacitance of **Porous-2** is lower than that of **Porous-1** at low current density, but the capacitance of **Porous-2** exceeds that of **Porous-1** at rates above 1 A/g, and retains a capacitance of 138 F/g at 10 A/g. Overall, **Porous-1** has higher capacitance at low cycle rates but **Porous-2** outperforms at higher rates.

These differences indicate a correlation between the structure and transport behavior of the materials. A power law is used to extract kinetic information from the CVs shown in Figure 3a−d. The peak current i_p is defined as

$$i_p = a \cdot v^b \tag{2}$$

where v is the scan rate, and a and b are constants. b typically ranges from 0.5 to 1, depending on whether the system is diffusion-limited or capacitive, respectively.[29,30] For **Porous-1**, $b \sim 0.9$ and ~ 0.6 for $v \leq 10$ mV/s and $v \geq 10$ mV/s, respectively, suggesting a surface-controlled capacitive behavior at low scan rate only (Figure S13). By contrast, $b \sim 1$ for **Porous-2** at scan rates up to 30 mV/s. At higher scan rates, $b \sim 0.7$, indicating contributions from both kinetic limits. Comparing both materials, it is clear that **Porous-2** maintains a larger degree of capacitive behavior at higher scan rates, supporting the conclusion that the cyclized scaffold shows faster diffusion kinetics than the uncyclized **Porous-1**. Though **Porous-2** is not formally fully conjugated, we have previously shown that the PDI-triptycene geometry exhibits through-space electron delocalization.[12]

The difference in performance for the two materials is a consequence of the molecular structure of the scaffold: cyclized **Porous-2** is more structurally rigid, allowing for faster ion transport kinetics. **Porous-1** and **Porous-2** both display high cycling stability with very little capacitance decay seen over 10 000 cycles at a current density of 5 A/g (Figure 4b). In fact, the capacitance of **Porous-1** increases slightly with cycling due to increased ion accessibility of the pores.

The frequency-dependent transport behavior of the materials was further investigated by electrochemical impe-
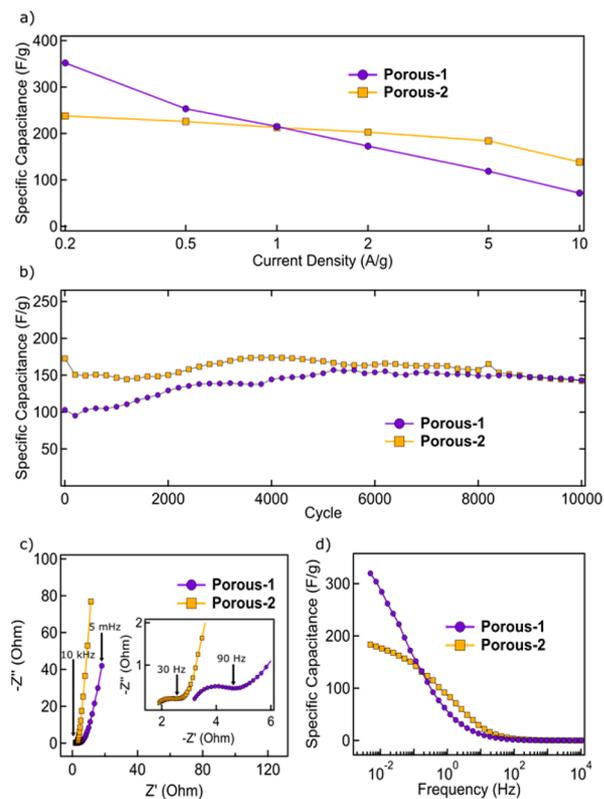
dance spectroscopy. The plots of the real (Z') versus imaginary (Z'') components of the impedance (Nyquist plots) for **Porous-1** and **Porous-2** are shown in Figure 4c. For both materials, a depressed semicircle representing the electrochemical reaction is observed at high frequency (inset of Figure 4c): both the charge transfer resistance, approximated from the diameter of the semicircle, and the internal resistance, approximated from the Z' intercept, are significantly lower for **Porous-2** than for **Porous-1**, supporting the faster kinetics of **Porous-2**.[12,31,32]

The low frequency linear response of the Nyquist plot represents the diffusion-limited processes. A slope (or phase shift) of 45° indicates a Warburg impedance[6,33,34] across a diffusive layer while a vertical line is expected for ideal double-layer capacitance.[35] The low frequency slope of **Porous-2** is steeper than that of **Porous-1**, also confirming its more capacitive nature.[1]

The specific capacitance of the materials as a function of frequency can be calculated[35] from the impedance data using a series circuit model:

$$C(f) = \frac{-1}{m \cdot Z'' \cdot 2\pi f} \tag{3}$$

where f is frequency (Figure 4d). At the lowest measured frequency of 5 mHz, the capacitance of **Porous-1** and **Porous-2** are 320 and 190 F/g, respectively, which are in very good agreement with the GCD results.

By copolymerizing redox-active PDI subunits with triptycene subunits, we have created a porous scaffold capable of n-type pseudocapacitor behavior. The electroactive scaffold exhibits outstanding performance with peak capacitance of 352 F/g and stability over >10 000 cycles. Moreover, we can tune the electrochemical and transport behavior of the material by modifying the structure postsynthesis. These results chart a clear path to expand the development of energy storage materials using molecular design.

ASSOCIATED CONTENT

Ⓢ Supporting Information

The Supporting Information is available free of charge on the ACS Publications website at DOI: 10.1021/jacs.8b07365.

Synthetic details, characterization, N_2 adsorption isotherms, mass spectrometry, IR spectroscopy, NMR spectroscopy, PXRD, SEM, UV/vis, CV, EIS, computational details (PDF)

AUTHOR INFORMATION

Corresponding Authors

*yy2664@columbia.edu
*xr2114@columbia.edu
*cn37@columbia.edu

ORCID Ⓘ

Samuel R. Peurifoy: 0000-0003-3875-3035
Yuan Yang: 0000-0003-0264-2640
Xavier Roy: 0000-0002-8850-0725
Colin Nuckolls: 0000-0002-0384-5493

Author Contributions

†S.R.P. and J.C.R. contributed equally.

Notes

The authors declare no competing financial interest.

REFERENCES

(1) Conway, B. E.; Birss, V.; Wojtowicz, J. *J. Power Sources* **1997**, *66* (1), 1−14.
(2) Nagaraju, G.; Raju, G. S. R.; Ko, Y. H.; Yu, J. S. *Nanoscale* **2016**, *8* (2), 812−825.
(3) Xiao, J.; Wan, L.; Yang, S.; Xiao, F.; Wang, S. *Nano Lett.* **2014**, *14* (2), 831−838.
(4) Kim, S. K.; Cho, J.; Moore, J. S.; Park, H. S.; Braun, P. V. *Adv. Funct. Mater.* **2016**, *26* (6), 903−910.
(5) Kou, Y.; Xu, Y.; Guo, Z.; Jiang, D. *Angew. Chem.* **2011**, *123* (37), 8912−8916.
(6) Arbizzani, C.; Catellani, M.; Mastragostino, M.; Mingazzini, C. *Electrochim. Acta* **1995**, *40* (12), 1871−1876.
(7) Bryan, A. M.; Santino, L. M.; Lu, Y.; Acharya, S.; D'Arcy, J. M. *Chem. Mater.* **2016**, *28*, 5989−5998.
(8) Mastragostino, M.; Arbizzani, C.; Soavi, F. *J. Power Sources* **2001**, *97*, 812−815.
(9) Vangari, M.; Pryor, T.; Jiang, L. *J. Energy Eng.* **2013**, *139* (2), 72−79.
(10) Long, T. M.; Swager, T. M. *J. Am. Chem. Soc.* **2002**, *124* (15), 3826−3827.
(11) Zhong, Y.; Kumar, B.; Oh, S.; Trinh, M. T.; Wu, Y.; Elbert, K.; Li, P.; Zhu, X.; Xiao, S.; Ng, F.; Steigerwald, M. L.; Nuckolls, C. *J. Am. Chem. Soc.* **2014**, *136* (22), 8122−8130.
(12) Peurifoy, S. R.; Castro, E.; Liu, F.; Zhu, X. Y.; Ng, F.; Jockusch, S.; Steigerwald, M. L.; Echegoyen, L.; Nuckolls, C.; Sisto, T. J. *J. Am. Chem. Soc.* **2018**, *140* (30), 9341.
(13) Milton, M.; Cheng, Q.; Yang, Y.; Nuckolls, C.; Hernández Sánchez, R.; Sisto, T. J. *Nano Lett.* **2017**, *17* (12), 7859−7863.
(14) Ghosh, I.; Ghosh, T.; Bardagi, J. I.; König, B. *Science* **2014**, *346* (6210), 725−728.
(15) Chandra, S.; Roy Chowdhury, D.; Addicoat, M.; Heine, T.; Paul, A.; Banerjee, R. *Chem. Mater.* **2017**, *29* (5), 2074−2080.
(16) Deblase, C. R.; Silberstein, K. E.; Truong, T. T.; Abruña, H. D.; Dichtel, W. R. *J. Am. Chem. Soc.* **2013**, *135* (45), 16821−16824.
(17) Schon, T. B.; McAllister, B. T.; Li, P.-F.; Seferos, D. S. *Chem. Soc. Rev.* **2016**, *45* (22), 6345−6404.
(18) Rajasingh, P.; Cohen, R.; Shirman, E.; Shimon, L. J.; Rybtchinski, B. *J. Org. Chem.* **2007**, *72* (16), 5973−5979.
(19) McKittrick, P.; Katon, J. *Appl. Spectrosc.* **1990**, *44* (5), 812−817.
(20) Sisto, T. J.; Zhong, Y.; Zhang, B.; Trinh, M. T.; Miyata, K.; Zhong, X.; Zhu, X. Y.; Steigerwald, M. L.; Ng, F.; Nuckolls, C. *J. Am. Chem. Soc.* **2017**, *139* (16), 5648−5651.
(21) Liu, X.; Cai, Y.; Huang, X.; Zhang, R.; Sun, X. *J. Mater. Chem. C* **2017**, *5* (12), 3188−3194.
(22) Bochevarov, A. D.; Harder, E.; Hughes, T. F.; Greenwood, J. R.; Braden, D. A.; Philipp, D. M.; Rinaldo, D.; Halls, M. D.; Zhang, J.; Friesner, R. A. *Int. J. Quantum Chem.* **2013**, *113* (18), 2110−2142.
(23) Tarazona, P.; Marconi, U. M. B.; Evans, R. *Mol. Phys.* **1987**, *60* (3), 573−595.

(24) Ryoo, R.; Kim, J. M.; Ko, C. H.; Shin, C. *J. Phys. Chem.* **1996**, *100* (45), 17718−17721.

(25) Zhao, D.; Feng, J.; Huo, Q.; Melosh, N.; Fredrickson, G. H.; Chmelka, B. F.; Stucky, G. D. *Science* **1998**, *279* (5350), 548−552.

(26) Kou, Y.; Xu, Y.; Guo, Z.; Jiang, D. *Angew. Chem., Int. Ed.* **2011**, *50* (37), 8753−8757.

(27) Snook, G. A.; Kao, P.; Best, A. S. *J. Power Sources* **2011**, *196* (1), 1−12.

(28) Li, H.; Wang, J.; Chu, Q.; Wang, Z.; Zhang, F.; Wang, S. *J. Power Sources* **2009**, *190* (2), 578−586.

(29) Augustyn, V.; Come, J.; Lowe, M. A.; Kim, J. W.; Taberna, P. L.; Tolbert, S. H.; Abruña, H. D.; Simon, P.; Dunn, B. *Nat. Mater.* **2013**, *12* (6), 518−522.

(30) Lindström, H.; Södergren, S.; Solbrand, A.; Rensmo, H.; Hjelm, J.; Hagfeldt, A.; Lindquist, S.-E. *J. Phys. Chem. B* **1997**, *101* (39), 7717−7722.

(31) Halme, J.; Toivola, M.; Tolvanen, A.; Lund, P. *Sol. Energy Mater. Sol. Cells* **2006**, *90* (7−8), 872−886.

(32) He, Z.; Mansfeld, F. *Energy Environ. Sci.* **2009**, *2* (2), 215−219.

(33) Ni, W.; Cheng, J.; Li, X.; Gu, G.; Huang, L.; Guan, Q.; Yuan, D.; Wang, B. *RSC Adv.* **2015**, *5* (12), 9221−9227.

(34) He, S.; Hou, H.; Chen, W. *J. Power Sources* **2015**, *280*, 678−685.

(35) Lee, J.-S. M.; Briggs, M. E.; Hu, C.-C.; Cooper, A. I. *Nano Energy* **2018**, *46*, 277−289.